

Simulation of Magnetospheric Sawtooth Oscillations: the Role of Kinetic Reconnection in the Magnetotail

Xiantong Wang¹, Yuxi Chen^{1,2}, Gábor Tóth¹

¹Department of Climate and Space Sciences and Engineering, University of Michigan, Ann Arbor, MI,
USA

²Now at Princeton Plasma Physics Laboratory, Princeton University, Princeton, NJ, USA

Key Points:

- The MHD with embedded particle-in-cell model is used to study sawtooth oscillations
- Kinetic reconnection in the magnetotail can produce sawtooth-like oscillations without varying ionospheric outflow

Corresponding author: Xiantong Wang, xtwang@umich.edu

Abstract

Magnetospheric sawtooth oscillations are observed during strong and steady solar wind driving conditions. The simulation results of our global MHD model with embedded kinetic physics show that when the total magnetic flux carried by constant solar wind exceeds a threshold, sawtooth-like magnetospheric oscillations are generated. Different from previous works, this result is obtained without involving time-varying ionospheric outflow in the model. The oscillation period and amplitude agree well with observations. The simulated oscillations cover a wide range of local times, although the distribution of magnitude as a function of longitude is different from observations. Our comparative simulations using ideal or Hall MHD models do not produce global time-varying features, which suggests that kinetic reconnection physics in the magnetotail is a major contributing factor to sawtooth oscillations.

Plain Language Summary

The magnetospheric sawtooth oscillation is a global-scale phenomenon in the Earth's magnetosphere. Observations and simulations suggest that the oxygen outflow from the ionosphere is inducing the sawtooth oscillations by affecting the rate of the magnetic reconnection: a fundamental physical process converting magnetic energy to plasma energy. We use a model where the magnetic reconnection is solved by kinetic physics and show that sawtooth-like oscillations can be induced if the incoming solar wind magnetic flux exceeds a threshold. This work proposes a new mechanism contributing to magnetospheric sawtooth oscillations.

1 Introduction

More than two decades ago, Borovsky et al. (1993) observed that the time variation of electron fluxes at geosynchronous orbit resemble a tooth of a saw blade: a slow decrease followed by a rapid increase. Moreover, this feature is observed in a wide range of magnetic local time (MLT), which distinguishes it from isolated substorms. These periodic injections also have impacts on other geospace features like magnetic field variations at geosynchronous orbit, the auroral electrojet index, and the polar cap index (Cai et al., 2006; Henderson et al., 2006; Huang et al., 2003). Although there is still no definitive answer to the mechanisms producing the sawtooth oscillations, numerical simulations for the coupled magnetosphere-ionosphere system have demonstrated a possible explanation related to the O^+ outflow from the ionosphere (Brambles et al., 2011). The basic idea of this theory is that the periodic mass loading and unloading from the ionospheric outflow alters the reconnection rate in the magnetotail current sheet. The different reconnection rate results in different magnetic field configuration in the tail, which modulates the ionospheric outflow rate. This feed back loop produces the periodic oscillations.

There are a number of studies establishing this theory over the past decade. Wiltberger et al. (2010) uses the Multi-Fluid Lyon Fedder Mobarry (MFLFM) model to demonstrate that the out-flowing cusp ions transported to the tail can have an effect on the magnetic configuration, and trigger substorm dipolarizations. Yu and Ridley (2013) also shows that cusp O^+ outflow can influence the development of isolated substorms. Brambles et al. (2011) applies an empirical power-law relationship between the Alfvénic Poynting flux and the resulting ionospheric outflow flux at the simulation inner boundary and shows that this outflow can induce quasi-periodic substorms resembling observed sawtooth oscillations. In a follow-up study, Ouellette et al. (2013) studies how the ion composition of the plasma sheet and magnetotail affects the tail reconnection rate. They hypothesized that the massive outflow inflates the magnetosphere and enables the development of the next sawtooth oscillation. Later on, Brambles et al. (2013) used the same model on two different types of sawtooth events induced by different external driving conditions:

62 the SIR-driven 24 October 2002 event and the CME-driven 18 April 2002 event. They
 63 find that quasi-periodic substorms occurred in the SIR event without outflow while no
 64 periodic substorm occurs in the CME event without outflow. Presumably, the quasi-periodic
 65 substorms in the SIR event are triggered by the variations in the external driving con-
 66 dition while in the CME event, they are more related to the internal mechanism of the
 67 magnetosphere. More recently, Lund et al. (2018) uses mass composition data from the
 68 Cluster satellites and discovers the role ionospheric outflow plays in inducing sawtooth
 69 oscillations. They find during the CME events, the O^+ in the mid-tail plasma sheet is
 70 mostly from the cusp/dayside while the nightside outflow preconditions the plasma sheet
 71 to enable the sawtooth oscillations. The recent work by Zhang et al. (2020) illustrates
 72 that magnetospheric sawtooth oscillations can be solely induced by cusp O^+ outflows
 73 in the global simulation conducted by the LFM model.

74 The previous publications all show that the magnetotail reconnection is the key factor
 75 in inducing the sawtooth oscillations and the ionospheric outflow is affecting the re-
 76 connection rate. In this paper, we use the University of Michigan’s Space Weather Mod-
 77 eling Framework (SWMF) (Tóth et al., 2012) to investigate how kinetic reconnection af-
 78 fects the sawtooth oscillations under constant solar wind driving conditions. In addition
 79 to the global MHD model simulating Earth’s magnetosphere, we are using the FLEKS
 80 (Flexible Exascale Kinetic Simulator) (Chen et al., 2021) in the magnetotail to model
 81 the tail reconnection with full kinetic physics. For comparison, we also present results
 82 by pure ideal MHD and Hall MHD models to emphasize the significance of the kinetic
 83 effects. Different from the previous work discussed above, we are not varying the plasma
 84 outflow from the ionosphere, hence the periodic oscillations observed are caused by the
 85 kinetic reconnection process embedded into the global MHD model.

86 The model description and simulation setup are described in section 2, the simu-
 87 lation results are presented in section 3 and we conclude in section 4.

88 2 Model Description and Simulation Setup

89 The simulations presented in this paper are conducted with the magnetohydrody-
 90 namics with embedded particle-in-cell (MHD-EPIC) model (Daldorff et al., 2014; Chen
 91 & Tóth, 2019). The MHD-EPIC model two-way couples the BATS-R-US MHD code (Powell
 92 et al., 1999; Tóth et al., 2008) and the semi-implicit particle-in-cell code FLEKS (Chen
 93 et al., 2021) through the Space Weather Modeling Framework (Tóth et al., 2012). The
 94 global magnetosphere structure is simulated by an ideal MHD model, with an embed-
 95 ded PIC region in the magnetotail to simulate the kinetic physics in the magnetic recon-
 96 nection. The ionospheric electrodynamics is simulated by the Ridley Ionosphere Model
 97 (RIM) (Ridley et al., 2004) that solves a Poisson-type equation for the electric poten-
 98 tial on a 2-D spherical grid, which is used to set the $\mathbf{E} \times \mathbf{B}$ velocity at the inner bound-
 99 ary of BATS-R-US. The MHD-EPIC model has been applied in studying multiple plan-
 100 etary and moon magnetospheres, such as the Earth (Chen et al., 2017, 2020), Mars (Ma
 101 et al., 2018), Mercury (Chen et al., 2019) and Ganymede (Tóth et al., 2016; Zhou et al.,
 102 2019, 2020).

103 A three-dimensional block-adaptive Cartesian grid of BATS-R-US is used to cover
 104 the entire computational domain: $-224R_E < x < 32R_E$ and $-128R_E < y, z < 128R_E$
 105 in GSM coordinates. The grid resolution is $1/4 R_E$ between $-60R_E < x < 20R_E$, $-20R_E <$
 106 $y < 20R_E$ and $-16R_E < z < 16R_E$. A shell region near the Earth from $2.5 R_E$ to
 107 $3.5 R_E$ is covered with $1/8 R_E$ grid resolution. The PIC box, the computational domain
 108 of FLEKS, is in the magnetotail between $-80R_E < x < -4R_E$, $-20R_E < y < 20R_E$
 109 and $-10R_E < z < 10R_E$ with grid resolution $1/4 R_E$. Figure 1 shows a 3-D overview
 110 of the simulation domain at $t = 3600$ s from the simulation presented in this paper. The
 111 color contour is the mass density on the equatorial plane, and the magnetic field lines

112 of two flux ropes are also plotted in the magnetotail. The black box is the PIC domain,
113 which covers the tail region where magnetic reconnection could happen.

114 To reduce the computational cost and make the simulation feasible, the speed of
115 light c is reduced to 15,000 km/s to speed up the convergence of the implicit solver, and
116 the ion-electron mass ratio m_i/m_e is decreased to 100 to increase the electron kinetic
117 scales. These modification have no direct impact on the results at the ion and global scales.
118 In addition to these numerical adjustments, we also scale up the ion and electron mass
119 per charge by a factor of 16 to increase the ion inertial length so that it can be resolved
120 with an affordable grid resolution. Tóth et al. (2017) presents theoretical arguments and
121 numerical experiments and concludes that (1) the solution of the equations is not sen-
122 sitive to the scaling at global scales and (2) the solution at the kinetic scale is propor-
123 tional to the scaling factor but will look the same.

124 The dipole tilt angle is set to 0° to form an idealized case. The inner boundary of
125 BATS-R-US is at $r = 2.5 R_E$, where the density is fixed at 28 amu/cc, the radial ve-
126 locity is set to 0, and the tangential velocity is calculated from the ionospheric $\mathbf{E} \times \mathbf{B}$
127 drift. Floating (zero-gradient) boundary condition is set for temperature and the mag-
128 netic field \mathbf{B}_1 that is the difference between the total field and the dipole. This bound-
129 ary condition does not prescribe ionospheric outflow, although plasma density is main-
130 tained at around 28 amu/cc and will be accelerated due to the external motional elec-
131 tric field in the open cusp region.

132 The solar wind condition applied at the inflow boundary of BATS-R-US is set to
133 constant to study the magnetosphere's response to an idealized ICME solar wind driv-
134 ing. We have two solar wind conditions: a) $V_x = -600$ km/s, IMF $B_z = -15$ nT for
135 strong driving and b) $V_x = -400$ km/s, IMF $B_z = -5$ nT for weak driving. The plasma
136 number density and the temperature of the solar wind are fixed at 5 cm^{-3} and 10^5 K,
137 respectively. The solar wind velocity components V_y, V_z and IMF components B_x, B_y
138 are all set to 0. Both strong and weak driving conditions are applied to the MHD-EPIC
139 model to demonstrate that exceeding a threshold of the transported magnetic flux from
140 the solar wind is necessary for triggering the sawtooth oscillation. We also run Hall MHD
141 and ideal MHD models under strong driving to emphasize the importance of the kinetic
142 reconnection.

143 We first run BATS-R-US and RIM for 15,000 steps using local time stepping with
144 ideal MHD until the system reaches a quasi-steady state. Then the time accurate mode
145 is turned on for 12 hours of physical time. The FLEKS model and/or the Hall MHD solver
146 are switched on in the time accurate section.

147 3 Results

148 3.1 Occurrence of sawtooth-like oscillations

149 A characteristic signature of sawtooth oscillations is the temporal variation of the
150 magnetic inclination angle, which is defined as the angle $\alpha = \arcsin(|B_z|/B)$ between
151 the magnetic field vector and the equatorial plane. Here B_z and B are the local mag-
152 netic field Z component and magnitude, respectively. The change of the magnetic in-
153 clination angle results from the field line stretching and dipolarization processes. At the
154 geostationary orbit, the average minimum inclination angle of an observed sawtooth is
155 26° as compared to 43° for the isolated substorms (Cai et al., 2006). Figure 2(a) shows
156 the magnetic inclination angles observed at $r = 8 R_E$ radial distance from the center
157 of Earth, 9° latitude and 2 am magnetic local time (MLT). The corresponding GSM co-
158 ordinates are $[x, y, z] = [-6.93, -4, 1.25] R_E$. Compared to the geostationary orbit, we
159 are observing further toward the magnetotail because the variations detected at $6.6 R_E$
160 are small. Due to the $\pm Z$ symmetry, the inclination angle is 90° in the equatorial plane,
161 so we extract values slightly above that plane. As we will see later, the largest variation

162 of the inclination angle occurs slightly off from the midnight direction, this is why we
 163 chose 2 am MLT.

164 The dashed gray line is the result of the ideal MHD model with strong solar wind
 165 driving, and the simulated magnetosphere takes about 2 hours to converge to a steady
 166 solution. There is no perturbation of the inclination angle, which stays at about 50° for
 167 the entire simulation. The solid gray line shows the result from the Hall MHD model with
 168 strong solar wind driving, which takes about 1.5 hours to reach a quasi-steady state. How-
 169 ever, unlike the ideal MHD model, the inclination angle oscillates around 60° with a $\pm 5^\circ$
 170 range. The difference in the average inclination angles between the ideal MHD and Hall
 171 MHD models can be explained by the different reconnection modes resulting from the
 172 two models. Simulations show that the ideal MHD gives a Sweet-Parker type solution
 173 while the Hall MHD model gives a solution closer to the Petschek type (Murphy et al.,
 174 2009). Though they are different in the values of inclination angles, it is clear that there
 175 are no sawtooth-like oscillations in the ideal and Hall MHD simulation results.

176 The MHD-EPIC result with strong solar wind driving is shown by the solid red line,
 177 while the result of weak solar wind driving is plotted in green. The MHD-EPIC run with
 178 weak solar wind driving shows similar oscillation to the Hall MHD run, although with
 179 a smaller average inclination angle around 55° . The MHD-EPIC run with strong solar
 180 wind driving shows different inclination angle variations from the other three runs. Af-
 181 ter about four hours of the simulation, the inclination angle drops to about 30° from 55°
 182 with a recovering phase afterward. There are three sawteeth shown in Figure 2 (a) and
 183 their starting times are marked by dashed vertical lines at $t = 4.15\text{h}, 5.38\text{h}$ and 7.15h .
 184 The third sawtooth shows a small dipolarization during the stretching phase. Partial dipo-
 185 larizations are consistent with observations as shown in the bottom panel of the figure.
 186 Panels (b) and (c) of Figure 2 compare the time variation of B_z from the MHD-EPIC
 187 simulation with strong solar wind driving and the observation from the POLAR satel-
 188 lite of the sawtooth event reported by Pulkkinen et al. (2006). The POLAR satellite tra-
 189 jectory is around $x = -8.0 R_E$ and $y = 3.5 R_E$ and moves from $-2 R_E$ to $2 R_E$ in GSM
 190 coordinate. The absolute values of B_z are different between the simulation and the ob-
 191 servation because they are acquired at different positions, but the differences between
 192 the maximum and the minimum B_z for each sawtooth are around 40 nT in both. Fur-
 193 thermore, a partial dipolarization was observed by POLAR between 17 : 00 and 18 :
 194 00 UT that is reminiscent of the simulation results between 9 and 10 hours.

195 From the four simulations with different setups presented in this section, we can
 196 conclude that two essential factors need to be satisfied for a global model to generate sawtooth-
 197 like oscillations without the time varying ionospheric outflow. First, the magnetic flux
 198 from the solar wind needs to exceed a certain threshold, which is also reported by (Cai
 199 et al., 2006) based on observations of many sawtooth events. Second, the tail reconec-
 200 tion needs to be simulated by the kinetic model.

201 3.2 Kinetic reconnection and sawtooth-like oscillations

202 In this subsection, we will investigate the connection between the sawtooth-like os-
 203 cillations shown in Figure 2 and the kinetic reconnection process in the magnetotail. Panel
 204 (a) of Figure 3 shows the magnetic field, particle energy, and half of the total energy in-
 205 side the PIC box normalized by the total energy at $t = 2\text{h}$. The electric field energy
 206 oscillates around 0.06% percent of the total energy, which is negligible compared to the
 207 energy of the magnetic field and the particles. The magnetic field and particles have a
 208 periodic energy gain/loss accompanied with the sawtooth oscillations.

209 Before $t = 4.4\text{h}$, there is no substantial energy transferred between the magnetic
 210 field and the particles. At $t \approx 4.4\text{h}$, the E_{magnetic} starts increasing while the E_{particle}
 211 starts decreasing. This stretching phase (S1) ends at $t \approx 5\text{h}$ when the difference reaches
 212 about 10%. In the next dipolarization phase (D1) the energy is transferred back from

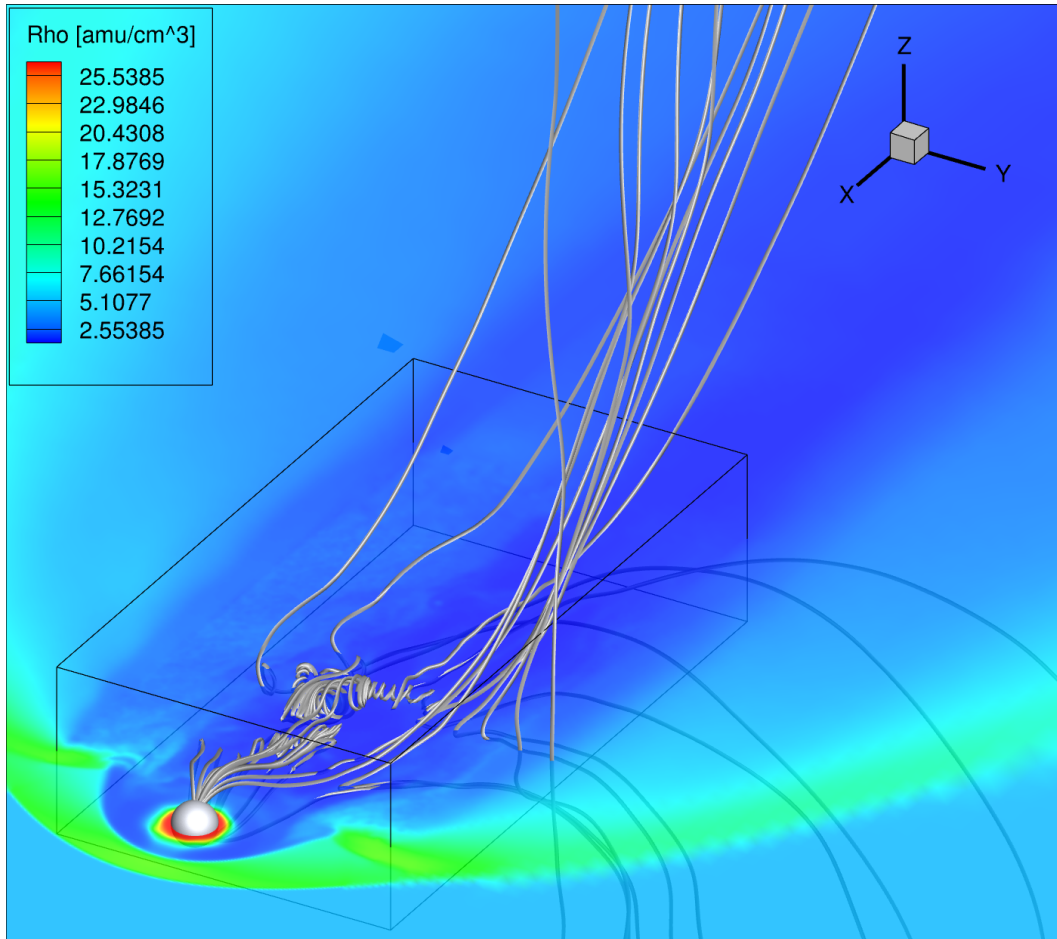


Figure 1. The global structure of Earth's magnetosphere at simulation time $t = 1$ h from the MHD-EPIC simulation with the strong solar wind driving condition. The color contour shows the mass density in the equatorial plane. The white spherical surface is the inner boundary at $2.5 R_E$. The gray rods are magnetic field lines of two flux ropes in the magnetotail. The black box is the domain of the PIC model that covers potential magnetic reconnection sites in the tail.

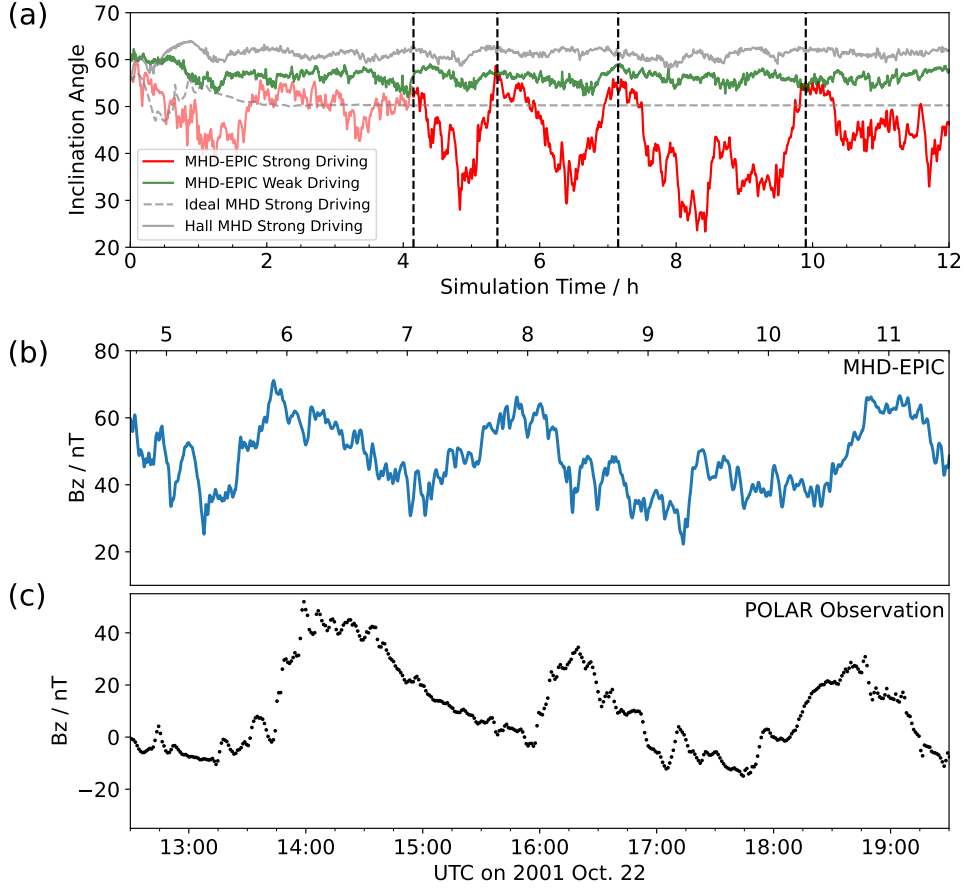


Figure 2. (a) Magnetic inclination angle plots from multiple simulations. MHD-EPIC with strong and weak solar wind driving conditions are shown in red and green. The ideal and Hall MHD results under strong solar wind driving are also plotted in gray for comparison. All inclination angles are taken at the same position: $x = -6.93 R_E$, $y = -4 R_E$ and $z = 1.25 R_E$. (b) Time variation of B_z at the same position from the MHD-EPIC simulation with strong driving. (c) Sawtooth event observations of B_z by the POLAR satellite from $(-8.0, 3.5, -2) R_E$ to $(-8.0, 3.5, 2) R_E$ in GSM coordinate. (Figure 3 from Pulkkinen et al. (2006)).

213 the magnetic field to the particles. The two parts of energy recover to the initial state
 214 at $t \approx 5.4$ h, which ends the first sawtooth period, and a similar oscillation starts at $t \approx$
 215 6 h and ends at $t \approx 7.5$ h (S2 and D2). Panels (b)-(e) of Figure 3 depict the electron
 216 kinetic energy multiplied by the sign of the X component of the electron velocity that
 217 is defined as $K_e = \frac{1}{2}\rho_e u_e^2 \text{sgn}(u_{e,x})$. The K_e values are plotted on the $B_x = 0$ isosur-
 218 face, which is the middle of the tail current sheet. We choose the electron kinetic energy
 219 because the electron features are well localized, and the sign change of K_e accurately in-
 220 dicates the position of the reconnection X line. The two blue vertical lines labeled S1
 221 and S2 in panel (a) are marked at $t = 4$ h 48min and $t = 6$ h 30min when E_{magnetic} reaches
 222 the maximum in each period and their corresponding E_k contour plots are shown in pan-
 223 els (b) and (d). In these panels, the magnetosphere is in a "stretching phase", when the
 224 X lines move towards the distant tail at $x \approx -40 R_E$. Another two red vertical lines
 225 labeled D1 and D2 in panel (a) are marked at $t = 5$ h 14min and $t = 7$ h 01min. Those
 226 two lines mark when E_{particle} (or E_{magnetic}) is increasing (or decreasing) most rapidly.
 227 Panels (c) and (e) show the corresponding E_k contour plots, when the magnetosphere
 228 is in a "dipolarization phase." In this phase, the X line is observed at $x \approx -15 R_E$ and
 229 the E_k near the X line is much larger. The "dipolarization phase" is also matching the
 230 recovery from the minimum inclination angle observed in Figure 2. The third sawtooth
 231 oscillation in the simulation is more complicated than the previous two. The dipolariza-
 232 tion phase is interrupted by a secondary stretching from $t \approx 8$ h 36min to $t \approx 9$ h 24min.
 233 The third oscillation fully recovers to the initial state at $t \approx 10$ h. The period of the os-
 234 cillations varies from 1.5 h to 3 h, which is very comparable with the observed period-
 235 icity.

236 3.3 Spatial distribution of the magnetic inclination angle

237 The wide extension of the variations of magnetic inclination angles in magnetic local
 238 time (MLT) is a critical signature of the sawtooth oscillations. Figure 4 shows the
 239 magnetic inclination contour plot from the MHD-EPIC simulation with strong solar wind
 240 driving conditions. The inclination angle is calculated along the circle $\sqrt{x^2 + y^2} = 7.9 R_E$
 241 in the plane $z = 1.26 R_E$ (the inclination angle is 90° in the $z = 0$ plane due to the
 242 symmetry of this idealized setup). The location we are looking at is further from the cen-
 243 ter of Earth than the observations at the geosynchronous orbit reported by Cai et al. (2006).
 244 Our MHD-EPIC simulation does not produce strong magnetic field perturbations at geosyn-
 245 chronous orbit. Despite the difference in the locations, the simulated inclination angle
 246 distribution over MLT exhibits several similarities compared to the observations. The
 247 minimum inclination angle from dawn to dusk is about 17° , which is close to observed
 248 sawtooth oscillations. The broad span in MLT also agrees with the observation. The stretch-
 249 ing and dipolarization phases with a period of around 1.5 hours are close to the observed
 250 periodicity.

251 While many features of the MHD-EPIC simulation results agree reasonably well
 252 with observations of sawtooth events (Cai et al., 2006), there are also several discrep-
 253 ancies. First, the signatures at the geosynchronous orbit are not strong enough to be ob-
 254 served, indicating that the stretching and dipolarization in the model are less energetic
 255 than in reality. Third, the stretching at midnight is much weaker than at dawn and dusk
 256 in the simulation. The observed sawtooth oscillations exhibit the lowest inclination an-
 257 gle near midnight and expand towards dawn and dusk. Third, the duration of each saw-
 258 tooth from the MHD-EPIC simulation varies from 1.5 to 3 hours, which is slightly shorter
 259 than a typically observed sawtooth that lasts from 2-4 hours.

260 One possible reason for the weaker signatures at midnight is that the "critical level"
 261 of the accumulated magnetic flux simulated by the MHD-EPIC model is lower than re-
 262 ality at dawn and dusk. The reconnection that happens there first causes stronger dipol-
 263 arization at dawn and dusk than observed, which dissipates the accumulated magnetic
 264 flux and preempts strong dipolarization at midnight.

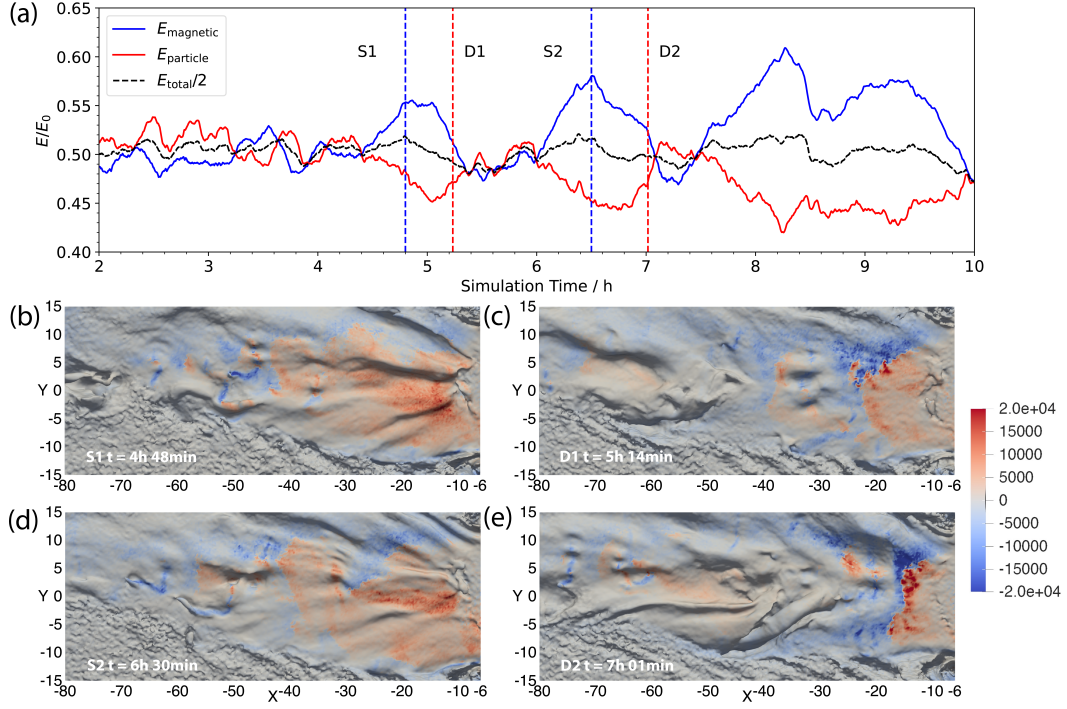


Figure 3. (a) The integrated magnetic field energy (blue) and particle energy (red) inside the PIC region normalized by the total energy at $t=2\text{h}$. The black line shows half of the normalized total energy. The four dashed vertical lines correspond to the times depicted by panels (b)-(e), respectively, during the stretching (S1 and S2) and dipolarization (D1 and D2) phases. These plots show the color contours of the electron kinetic energy multiplied by the sign of the X component of the electron velocity: $K_e = \frac{1}{2}\rho_e u_e^2 \text{sgn}(u_{e,x})$. The color contour is plotted on the $B_x = 0$ isosurface that identifies the middle of the magnetotail current sheet. Sharp jumps from dark blue to dark red color indicate reconnection jets emanating from the X-lines. The black shadows show that the current sheet surface is rippled.

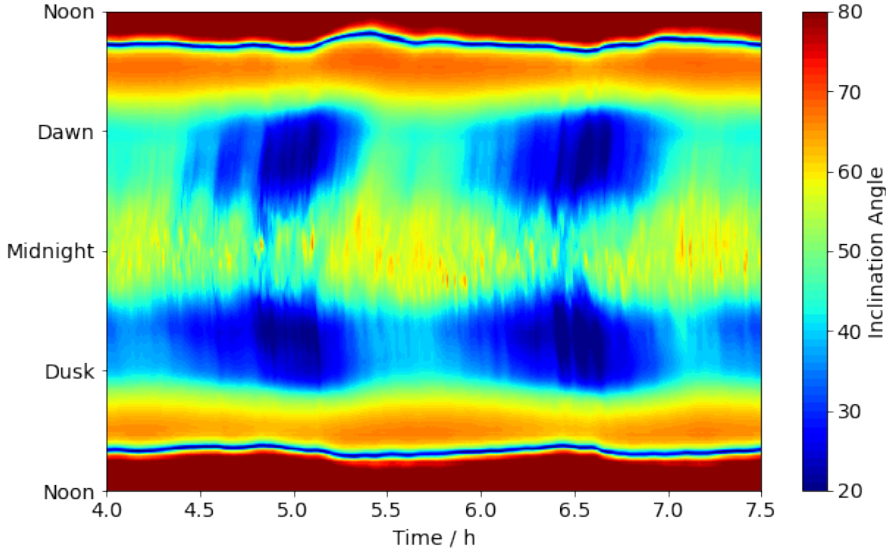


Figure 4. The contour plot of the magnetic inclination angle of the first two sawteeth from the MHD-EPIC simulation with strong solar wind driving. The inclination angle is evaluated on the circle $\sqrt{x^2 + y^2} = 7.9 R_E$ in the plane $z = 1.26 R_E$, which is outside the geosynchronous orbit.

4 Conclusion and Discussion

In this paper, we use the MHD with Embedded Particle-In-Cell (MHD-EPIC) model to study the role kinetic reconnection plays in generating magnetospheric sawtooth events. The PIC region covers a box region in the magnetotail where the reconnection could potentially happen. Different from prior MHD simulations of sawtooth events, there is no time varying ionospheric outflow transporting plasma to the magnetotail. We apply both strong and weak solar wind driving conditions in the MHD-EPIC simulations to demonstrate that the occurrence of the sawtooth oscillations depends on the incoming rate of the magnetic flux from the solar wind. To emphasize the significance of the kinetic model, we also perform the simulation using ideal MHD and Hall MHD models with the strong solar wind driving conditions for comparison.

We examine the temporal variation of the magnetic inclination angle in the near tail at $(x, y, z) = (-6.93, -4, 1.25) R_E$ from different simulations. We find that only the MHD-EPIC model with strong solar wind driving condition produces periodic oscillations of the magnetic inclination angle that has a minimum value below 30° , which demonstrates that both the kinetic magnetic reconnection and the incoming rate of the magnetic flux from the solar wind are essential to induce the sawtooth oscillations. We investigate the variations of magnetic and particle energy from the MHD-EPIC simulation. The energy is transferred from the particles to the magnetic field during the stretching phase. When the dipolarization starts, the energy transfers in the opposite direction. We also plot the electron kinetic energy contour on the current sheet surface, and we observe that the dipolarization phase of the sawtooth oscillation is related to the formation of a reconnection X-line close to the Earth. We find that the oscillations from the MHD-EPIC simulation exhibit a wide span over the magnetic local time that is a signature of observed sawtooth events. However, there are three major discrepancies between the MHD-EPIC generated sawtooth oscillations and the observations: 1. the sig-

291 nature at the geosynchronous orbit is relatively weak. 2. the simulated period of the saw-
 292 tooth oscillations varies from 1.5 to 3 hours that is somewhat shorter than the observed
 293 periods of 2 to 4 hours. 3. the minimum inclination angle in the simulation is found at
 294 the dawn and dusk regions rather than at midnight.

295 We suggest that the kinetic reconnection in the magnetotail can solely reproduce
 296 the periodic loading and unloading process of the magnetic flux in the magnetosphere.
 297 The reconnection rate in the magnetotail is not high enough to dissipate the incoming
 298 magnetic flux from the solar wind. Thus the imbalance between the dayside and night-
 299 side causes the magnetic flux to accumulate towards a critical level on the nightside and
 300 triggers dipolarization. This process is recognized as the direct causing mechanism of the
 301 sawtooth oscillations (Zhang et al., 2020). Hence we conclude that in addition to the iono-
 302 spheric outflow, the sawtooth oscillations might be an intrinsic feature of the kinetic re-
 303 connection in the magnetotail when the incoming magnetic flux from the solar wind ex-
 304 ceeds a threshold. However, the discrepancies between the observation and the MHD-
 305 EPIC simulation suggest that ionospheric outflow is also an important factor. The iono-
 306 spheric O^+ transported into the magnetotail will change the plasma mass density and
 307 composition, which may make the stretching phase last longer. Also, the "precondition-
 308 ing" by the nightside outflow mentioned by Zhang et al. (2020) might reduce the discrep-
 309 ancy at the midnight sector between the MHD-EPIC simulation and observations. In
 310 future work, we believe it is important to include both ionospheric outflow and kinetic
 311 magnetic reconnection physics in the magnetotail to fully understand sawtooth oscilla-
 312 tions.

313 Data Availability Statement

314 The POLAR satellite data is obtained from the Coordinated Data Analysis Web
 315 (CDAWeb) from NASA. The SWMF code (including BATS-R-US and FLEKS) is pub-
 316 licly available through the csem.engin.umich.edu/tools/swmf web site after registration.
 317 The simulation output and scripts used for generating figures in this paper can be ob-
 318 tained online through the University of Michigan's Deep Blue Data repository, which is
 319 specifically designed for U-M researchers to share their research data and to ensure its
 320 long-term viability.

321 Acknowledgments

322 This work was primarily supported by NSF PRE-EVENTS grant No. 1663800. We also
 323 acknowledge support from the NASA DRIVE Center at the University of Michigan un-
 324 der grant NASA 80NSSC20K0600. We acknowledge the Texas Advanced Computing Cen-
 325 ter (TACC) at The University of Texas at Austin for providing HPC and storage resources
 326 that have contributed to the research results reported within this paper.

327 References

- 328 Borovsky, J., Nemzek, R. J., & Belian, R. D. (1993). The occurrence rate of
 329 magnetospheric-substorm onsets: Random and periodic substorms. *J. Geo-*
 330 *phys. Res.*, *98*, 3807–3813.
- 331 Brambles, O., Lotko, W., Zhang, B., Ouellette, J., Lyon, J., & Wiltberger, M.
 332 (2013). The effects of ionospheric outflow on icme and sir driven sawtooth
 333 events. *Journal of Geophysical Research: Space Physics*, *118*(10), 6026–6041.
- 334 Brambles, O., Lotko, W., Zhang, B., Wiltberger, M., Lyon, J., & Strangeway, R.
 335 (2011). Magnetosphere sawtooth oscillations induced by ionospheric outflow.
 336 *Science*, *332*(6034), 1183–1186.
- 337 Cai, X., Clauer, C., & Ridley, A. (2006). Statistical analysis of ionospheric poten-
 338 tial patterns for isolated substorms and sawtooth events. *Ann. Geophys.*, *24*,

- 339 1977.
- 340 Chen, Y., & Tóth, G. (2019). Gauss's law satisfying energy-conserving semi-implicit
341 particle-in-cell method. *J. Comput. Phys.*, *386*, 632. doi: 10.1016/j.jcp.2019.02
342 .032
- 343 Chen, Y., Tóth, G., Cassak, P., Jia, X., Gombosi, T. I., Slavin, J., ... Peng,
344 B. (2017). Global three-dimensional simulation of earth's dayside recon-
345 nection using a two-way coupled magnetohydrodynamics with embedded
346 particle-in-cell model: initial results. *J. Geophys. Res.*, *122*, 10318. doi:
347 10.1002/2017JA024186
- 348 Chen, Y., Toth, G., Zhou, H., & Wang, X. (2021). Fleks: A flexible particle-in-
349 cell code for multi-scale plasma simulations. *Earth and Space Science Open*
350 *Archive*. doi: doi.org/10.1002/essoar.10508070.1
- 351 Chen, Y., Tóth, G., Hietala, H., Vines, S. K., Zou, Y., Nishimura, Y., ... Markidis,
352 S. (2020). Magnetohydrodynamic with embedded particle-in-cell simulation of
353 the geospace environment modeling dayside kinetic processes challenge event.
354 *Earth and Space Science*, *7*(11), e2020EA001331. Retrieved from [https://](https://agupubs.onlinelibrary.wiley.com/doi/abs/10.1029/2020EA001331)
355 agupubs.onlinelibrary.wiley.com/doi/abs/10.1029/2020EA001331 doi:
356 <https://doi.org/10.1029/2020EA001331>
- 357 Chen, Y., Tóth, G., Jia, X., Slavin, J. A., Sun, W., Markidis, S., ... Raines, J. M.
358 (2019). Studying dawn-dusk asymmetries of mercury's magnetotail using mhd-
359 epic simulations. *Journal of Geophysical Research: Space Physics*, *124*(11),
360 8954-8973.
- 361 Daldorff, L. K. S., Tóth, G., Gombosi, T. I., Lapenta, G., Amaya, J., Markidis, S., &
362 Brackbill, J. U. (2014). Two-way coupling of a global Hall magnetohydrody-
363 namics model with a local implicit Particle-in-Cell model. *J. Comput. Phys.*,
364 *268*, 236. doi: 10.1016/j.jcp.2014.03.009
- 365 Henderson, M., Reeves, G., Skoug, R., Thomsen, M., Denton, M. H., Mende, S.,
366 ... Singer, H. (2006). Magnetospheric and auroral activity during the 18
367 april 2002 sawtooth event. *Journal of Geophysical Research: Space Physics*,
368 *111*(A1).
- 369 Huang, C.-S., Reeves, G., Borovsky, J., Skoug, R., Pu, Z., & Le, G. (2003). Periodic
370 magnetospheric substorms and their relationship with solar wind variations.
371 *Journal of Geophysical Research: Space Physics*, *108*(A6).
- 372 Lund, E. J., Nowrouzi, N., Kistler, L. M., Cai, X., & Frey, H. U. (2018). On the role
373 of ionospheric ions in sawtooth events. *Journal of Geophysical Research: Space*
374 *Physics*, *123*(1), 665-684.
- 375 Ma, Y., Russell, C. T., Toth, G., Chen, Y., Nagy, A. F., Harada, Y., ... others
376 (2018). Reconnection in the martian magnetotail: Hall-mhd with embedded
377 particle-in-cell simulations. *Journal of Geophysical Research: Space Physics*,
378 *123*(5), 3742-3763.
- 379 Murphy, N., Sovinec, C., & Cassak, P. (2009). Simulation and analysis of magnetic
380 reconnection in an experimental geometry. In *Bulletin of the american astro-*
381 *nomical society* (Vol. 41, p. 514).
- 382 Ouellette, J., Brambles, O., Lyon, J., Lotko, W., & Rogers, B. (2013). Properties
383 of outflow-driven sawtooth substorms. *Journal of Geophysical Research: Space*
384 *Physics*, *118*(6), 3223-3232.
- 385 Powell, K., Roe, P., Linde, T., Gombosi, T., & De Zeeuw, D. L. (1999). A solution-
386 adaptive upwind scheme for ideal magnetohydrodynamics. *J. Comput. Phys.*,
387 *154*, 284-309. doi: 10.1006/jcph.1999.6299
- 388 Pulkkinen, T., Ganushkina, N. Y., Tanskanen, E., Kubyshkina, M., Reeves, G.,
389 Thomsen, M., ... Gjerloev, J. (2006). Magnetospheric current systems during
390 stormtime sawtooth events. *Journal of Geophysical Research: Space Physics*,
391 *111*(A11).
- 392 Ridley, A., Gombosi, T., & Dezeew, D. (2004, February). Ionospheric control of the
393 magnetosphere: conductance. *Annales Geophysicae*, *22*, 567-584. doi: 10.5194/

- 394 angeo-22-567-2004
- 395 Tóth, G., Chen, Y., Gombosi, T. I., Cassak, P., Markidis, S., & Peng, B. (2017).
396 Scaling the ion inertial length and its implications for modeling reconnection in
397 global simulations. *J. Geophys. Res.*, *122*, 10336. doi: 10.1002/2017JA024189
- 398 Tóth, G., Jia, X., Markidis, S., Peng, B., Chen, Y., Daldorff, L., . . . Dorelli, J.
399 (2016). Extended magnetohydrodynamics with embedded particle-in-cell
400 simulation of ganymede’s magnetosphere. *J. Geophys. Res.*, *121*. doi:
401 10.1002/2015JA021997
- 402 Tóth, G., Ma, Y. J., & Gombosi, T. I. (2008). Hall magnetohydrodynamics on block
403 adaptive grids. *J. Comput. Phys.*, *227*, 6967-6984. doi: 10.1016/j.jcp.2008.04
404 .010
- 405 Tóth, G., van der Holst, B., Sokolov, I. V., Zeeuw, D. L. D., Gombosi, T. I., Fang,
406 F., . . . Opher, M. (2012). Adaptive numerical algorithms in space weather
407 modeling. *J. Comput. Phys.*, *231*, 870–903. doi: 10.1016/j.jcp.2011.02.006
- 408 Wiltberger, M., Lotko, W., Lyon, J. G., Damiano, P., & Merkin, V. (2010). In-
409 fluence of cusp o+ outflow on magnetotail dynamics in a multifluid mhd
410 model of the magnetosphere. *J. Geophys. Res.*, *115*(A10), 148-227. doi:
411 10.1029/2010JA015579
- 412 Yu, Y., & Ridley, A. J. (2013). Exploring the influence of ionospheric o+ outflow on
413 magnetospheric dynamics: dependence on the source location. *Journal of Geo-*
414 *physical Research: Space Physics*, *118*(4), 1711–1722.
- 415 Zhang, B., Brambles, O. J., Lotko, W., & Lyon, J. G. (2020). Is nightside outflow
416 required to induce magnetospheric sawtooth oscillations. *Geophysical Research*
417 *Letters*, *47*(6), e2019GL086419.
- 418 Zhou, H., Tóth, G., Jia, X., & Chen, Y. (2020). Reconnection-driven dynam-
419 ics at ganymede’s upstream magnetosphere: 3-d global hall mhd and mhd-
420 epic simulations. *Journal of Geophysical Research: Space Physics*, *125*(8),
421 e2020JA028162.
- 422 Zhou, H., Tóth, G., Jia, X., Chen, Y., & Markidis, S. (2019). Embedded kinetic sim-
423 ulation of ganymede’s magnetosphere: Improvements and inferences. *Journal*
424 *of Geophysical Research: Space Physics*, *124*(7), 5441–5460.